Size-dependent dynamic structures of supported gold nanoparticles in CO oxidation reaction condition

Yang He[a,1], Jin-Cheng Liu[b,c,1], Langli Luo[d,1], Yang-Gang Wang[b,c], Junfa Zhu[e,f], Yingge Du[g], Jun Li (李 隽)[b,c,d,2], Scott X. Mao[a,2], and Chongmin Wang[d,2]

[a]Department of Mechanical Engineering and Materials Science, University of Pittsburgh, Pittsburgh, PA 15261; [b]Department of Chemistry, Tsinghua University, Beijing 100084, China; [c]Key Laboratory of Organic Optoelectronics and Molecular Engineering of the Ministry of Education, Tsinghua University, Beijing 100084, China; [d]Environmental Molecular Sciences Laboratory, Pacific Northwest National Laboratory, Richland, WA 99354; [e]National Synchrotron Radiation Laboratory, University of Science and Technology China, Hefei, Anhui 230029, China; [f]Department of Chemical Physics, University of Science and Technology China, Hefei, Anhui 230029, China; and [g]Physical and Computational Sciences Directorate, Pacific Northwest National Laboratory, Richland, WA 99354

Edited by Catherine J. Murphy, University of Illinois at Urbana–Champaign, Urbana, IL, and approved June 12, 2018 (received for review January 5, 2018)

Gold (Au) catalysts exhibit a significant size effect, but its origin has been puzzling for a long time. It is generally believed that supported Au clusters are more or less rigid in working condition, which inevitably leads to the general speculation that the active sites are immobile. Here, by using atomic resolution in situ environmental transmission electron microscopy, we report size-dependent structure dynamics of single Au nanoparticles on ceria (CeO_2) in CO oxidation reaction condition at room temperature. While large Au nanoparticles remain rigid in the catalytic working condition, ultrasmall Au clusters lose their intrinsic structures and become disordered, featuring vigorous structural rearrangements and formation of dynamic low-coordinated atoms on surface. Ab initio molecular-dynamics simulations reveal that the interaction between ultrasmall Au cluster and CO molecules leads to the dynamic structural responses, demonstrating that the shape of the catalytic particle under the working condition may totally differ from the shape under the static condition. The present observation provides insight on the origin of superior catalytic properties of ultrasmall gold clusters.

gold catalysis | size effect | adsorbate-induced disorder | dynamic low-coordinated atoms

The discovery of catalytic properties of gold (Au) is a landmark in catalysis science (1, 2). The observation of supported Au nanoparticles (NPs) of ∼2–5 nm possessing robust catalytic properties (3, 4) has triggered extensive studies of Au heterogeneous catalysts (5–9). Consequently, it has been generally realized that only nanosized Au particles are active (1, 7, 8), and their reactivities are highly size dependent (8, 10). However, the origin of such a significant size effect and the associated catalytic mechanism remain as the biggest puzzle (8, 9). It was suggested that the atoms on the metal-support interface were the active sites (5), and hence the size dependence would be directly related to the ratio of the perimeter sites to the particle size. However, this picture relies on the contention that, under the working condition, the Au NP is more or less rigid, such that the atoms at the interior of the particle would hardly participate in the reactions or remain inactive (11–14). However, in situ studies in recent years have revealed otherwise, that the surface structures of supported metallic NPs (15–18), including the noblest gold metal (19), are not rigid. Takeda and coworkers (20, 21) explored Au NP catalyst supported on TiO_2 and CeO_2 under various gas conditions and found that the Au NPs with a size of 2∼5 nm remain as face-centered cubic (FCC) structure but undergo surface restructuring under high O_2/CO ratio or upon adsorption of CO molecules on Au surface. Other in situ experimental studies also revealed that CO can etch the surface of bulk Au by relocating the atoms to form clusters (11, 13). As Au particle sizes further decrease, the ratio of surface atoms dramatically increases; and hence the ultrasmall cluster may completely lose its structure stability due to the interaction between the surface atoms and CO molecules. Nonetheless, in situ study on ultrasmall (<2-nm) supported Au clusters in reaction condition is still lacking to date, which is critical in unveiling the origin of size effect in ultrasmall Au catalysis.

Here, through state-of-the-art aberration-corrected environmental transmission electron microscopy (ETEM) and a unique in situ experiment setup (see *Methods* and *SI Appendix*, Fig. S1*A*, for details), we directly captured the structure evolution of individual Au NPs [supported on CeO_2(111) surface] under catalytic working condition. The sizes of Au NPs rang from ∼2-nm-sided hexagonal single layers (in which all atoms are literally on surface) to NPs of 4∼5 nm in diameter. We find that, upon exposing to reactant gases ($CO + O_2$) at room temperature, the structures of ultrasmall Au clusters were dramatically changed, featuring a transition from FCC structure to dynamic disordered structure and with Au (presumably Au′CO) atoms dynamically stretching out of the particle surface to form dynamic low-coordinated atoms (DLCAs). In contrast, large Au NPs remained rigid in FCC structure with typical surface reconstruction. The size-dependent dynamic structural changes and generation

Significance

Gold is the noblest metal. However, when the size decreases to nanoscale and is supported on reducible oxides, the gold nanoparticle shows exceptionally high catalytic performance even at low temperatures. Here, through state-of-the-art in situ aberration-corrected environmental transmission electron microscopy and ab initio molecular-dynamic simulations, we discovered that, upon exposing to reactant gas (carbon monoxide and oxygen), ultrasmall gold clusters on ceria show a size-dependent order-to-disorder transformation with generation of dynamic low-coordinated atoms, which presumably can effectively boost the oxidation reaction of carbon monoxide. The findings provide much-needed insights on the origin of size-dependent catalytic properties of supported gold and demonstrate a size effect in absorbent–particle interactions that may widely exist and play an essential role in heterogeneous catalysts.

Author contributions: J.L., S.X.M., and C.W. designed research; Y.H., J.-C.L., L.L., Y.-G.W., J.Z., and Y.D. performed research; Y.H., J.-C.L., and L.L. analyzed data; and Y.H., J.-C.L., J.L., S.X.M., and C.W. wrote the paper.

The authors declare no conflict of interest.

This article is a PNAS Direct Submission.

Data deposition: The data that support the findings of this study are provided in the manuscript, are kept at the Environmental Molecular Sciences Laboratory at Pacific Northwest National Laboratory, and are available from the corresponding authors on request.

[1]Y.H., J.-C.L., and L.L. contributed equally to this work.

[2]To whom correspondence may be addressed. Email: junli@tsinghua.edu.cn, sxm2@pitt.edu, or chongmin.wang@pnnl.gov.

This article contains supporting information online at www.pnas.org/lookup/suppl/doi:10.1073/pnas.1800262115/-/DCSupplemental.

Published online July 9, 2018.

of DLCAs in ultrasmall Au clusters were corroborated by our ab initio molecular-dynamics (AIMD) simulations, which further revealed that the generation of DLCA via gold-carbonyl (Au′CO) species could act as dynamic active centers for CO oxidation. Therefore, the observation of size-dependent dynamic structures of supported Au NPs under CO provides insights on the long-debated origin of the size-dependent catalytic properties of gold.

Results and Discussion

The dynamic structural changes of the Au NPs (with three different sizes) upon exposing to the reactant gases are represented in Fig. 1. The reaction condition used a gas mixture of CO and O_2 (volume ratio, 2:1) at 10^{-3} to $\sim 10^{-4}$ mbar and room temperature. In vacuum, all three Au NPs were in FCC structure. Upon exposing them to the reactant gases, however, they showed distinct size-dependent dynamic structures. The large (4-nm) NP (Fig. 1 *A*–*C*) remained almost intact except for a well-known reconstruction of Au(100) surface as a result of CO adsorption (*SI Appendix*, Fig. S1 *B* and *C* and Movie S1) (21). In direct contrast, the smaller Au NPs showed dramatic structural changes. The Au NP with size of <2 nm lost its FCC structure and became disordered in the reaction condition (Fig. 1 *D*–*F* and Movie S2), as evidenced by the high-resolution transmission electron microscopy (HRTEM) image and ring feature of the fast Fourier transform (Fig. 1*F*). Similarly, upon exposing to reactant gases, the Au single layer (SL) wrapped up to a 3D "onion-like" structure as shown in Fig. 1 *G*–*I* and Movie S3.

We further found that, under reaction condition, the smaller Au NPs showed dynamic structural changes as represented by the HRTEM snapshots in Fig. 2. Compared with that in the 4-nm Au NP (*SI Appendix*, Fig. S1 and Movie S1), atoms in the <2-nm Au NP were much mobile under the reaction condition, as manifested by the continuously evolving disordered structure of the NP (Fig. 2*A* and Movie S2). The flexibility of atoms near the perimeter was much higher overall; within the interval of a general structure change of the whole particle, atoms in the vicinity of the perimeter could form DLCAs as manifested by atoms stretching out of the Au NP surface and formation of "single atoms" on the Au/CeO_2 perimeter (Fig. 2*B*). The contrasts of the disordered structure and DLCAs were verified by HRTEM image simulations based on the model structure of a CO-adsorbed Au NP after relaxation using density functional theory (DFT) (*SI Appendix*, Fig. S2). The continuously evolving disordered structure under working condition was also found in the cluster evolved from the Au SL (Movie S3).

To unveil the key factors that are responsible for these structure changes, we carried out several control experiments with reactant gases that include pure CO and argon under the identical gas pressure and temperature as for the case of CO + O_2 and controlled imaging-beam condition. The dynamic structural changes also happened in pure CO under beam-blank condition, but not in argon (*SI Appendix*, Fig. S3). These results indicate that the observed dynamic structural changes of Au NPs should be attributed to CO adsorption, which has been predicted based on AIMD and DFT calculations and spectroscopic

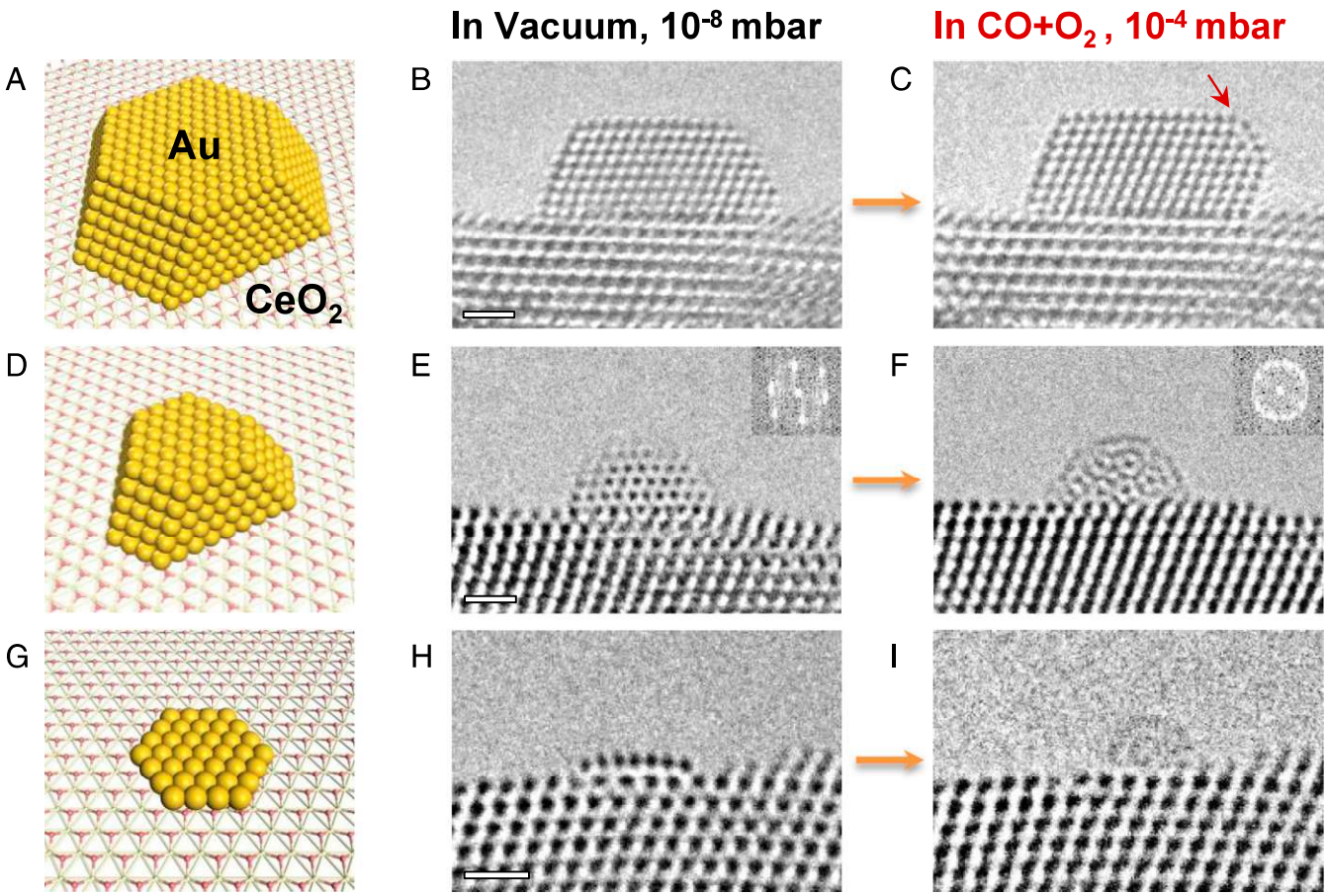

Fig. 1. Dynamic structural changes of various Au nanostructures supported on CeO_2(111) upon exposing to the reactant gases. (*A*–*C*) Model (*A*) and HRTEM images (*B* and *C*) of a 4-nm Au NP with ~1,000 atoms; the arrow in *C* indicates the Au(100) surface reconstruction. (*D*–*F*) The <2-nm Au NP with 100~200 atoms; the *Insets* show corresponding fast Fourier transform of the Au NP. (*G*–*I*) The ~2-nm SL with ~40 atoms. (Scale bars: *B*, *E*, and *H*, 1 nm; also apply to *C*, *F*, and *I*, respectively.)

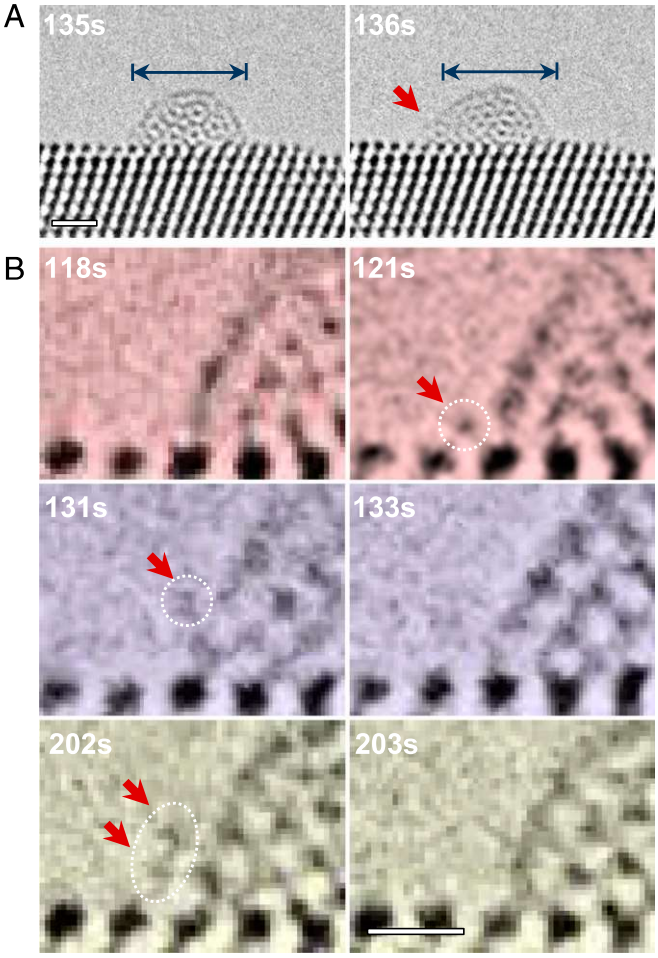

Fig. 2. Dynamic structure changes of the <2-nm Au NP under reaction condition. (*A*) Continuous structural changes of the Au NP (the double arrow serves as a reference to indicate the liquid-like flow of atoms within 1 s). (*B*) Enlarged HRTEM images showing that Au atoms in the vicinity of Au/CeO_2 contact were dynamically stretched out forming dynamic low-coordinated atoms (DLCAs) (indicated by red arrows and dashed circles) on Au surface and Au/CeO_2 perimeter. (Scale bars: *A*, 1 nm; *B*, 500 pm.)

observation (10, 12, 22), but has never been directly observed previously.

The atomic-scale mechanisms that underpin the observed size-dependent structural dynamics of Au NP in reaction condition were provided by our first-principles DFT calculations combined with AIMD simulations. In doing so, we chose both Au SLs and Au NPs that are represented by those shown in Fig. 1. We selected Au_{19} SL with 12 adsorbed CO molecules supported on CeO_2(111) surface as the initial structure for AIMD simulations (Fig. 3*A*). Note that a surface oxygen vacancy was used to stabilize the Au_{19} SL (23, 24). After ∼25-ps evolution, the original SL lost its hexagonal configuration and transformed to 3D clusters, which is primarily caused by extraction and motion of Au atoms in the form of Au′CO species (Fig. 3*B*), while isolated Au_{19} or supported CO-free Au_{19} SLs maintained hexagonal SL configuration within the simulation time span at 300 K (*SI Appendix*, Figs. S4 and S5). This single layer-to-3D cluster transition was further confirmed by the calculation of distance distribution of Au atoms relative to the mass center of the cluster (Fig. 3*C*), where both supported and unsupported Au_{19} maintained hexagonal SL structures as manifested by three well-defined peaks (at 2.8, 4.9, and 5.6 Å for three kinds of Au atoms), while these three peaks all disappeared in Au_{19} with CO adsorption, suggesting a collapse of the SL and formation of disordered structure as shown in the Movies S4 and S5 (12). The AIMD simulation on the behavior of Au SL is fairly consistent with our experimental observations in Fig. 1.

Moreover, the dynamic behavior of the supported Au cluster mainly involves breaking and formation of Au–Au bonds, while the stronger Au–CO bonds are relatively stable (Fig. 3*B*), indicating that the transport of CO on Au cluster is based on Au′CO species. The diffusion barrier for Au′CO species on Au cluster is estimated to be ∼0.07 eV, by the potential of mean force $V(r) = -k_BT\ln(g(r))$, where $g(r)$ is the radial distribution function (Fig. 3*D*). This barrier is significantly lower than the reported barrier (∼0.6 eV) for the diffusion of CO on FCC Au (22) but is well consistent with the barrier of Au′CO diffusion on Au(111) surface or supported Au SL (*SI Appendix*, Fig. S6). This facile transport of Au′CO species was also evidenced by the fact that Au′CO species was stretched out of the Au cluster and migrated to the surface oxygen site to form O_{surf}–Au–CO (Fig. 3*B*, green ball), which is a thermodynamically favorable process. The agile Au′CO species agree well with our experimental observations on formation of DLCAs in Fig. 2.

Since CO adsorption-induced Au′CO extraction plays an essential role for the observed order-to-disorder transformation and is likely responsible for formation of DLCA, we further evaluated the size dependence of the energies and barriers for this process (Fig. 3*E*). Compared with that on the edge of bulk Au, formation energies of Au′CO (or DLCA) at the edges of supported Au nanorod and SL are much lower, even with negative values (*SI Appendix*, Fig. S6). When two COs adsorb on adjacent Au sites, the energy barriers for Au′CO extraction on supported Au nanorod and SL are 0.04 and 0.29 eV, respectively; whereas the barrier for the same process on bulk Au(111)/(111) edge is much higher (∼0.92 eV), manifesting that smaller Au NPs are more susceptible to Au′CO extraction.

Furthermore, the calculated coverage-dependent adsorption energy per CO molecule on Au NPs linearly decreases with increasing particle size, leading to a considerable decrease of CO coverage with increasing Au particle size (*SI Appendix*, Fig. S7). The low coverage of large NPs can be attributed to the decrease of edges and apexes sites where CO is more likely to adsorb (25–27). Mpourmpakis and coworkers (28) recently reported that the average binding energy of CO on Au increases exponentially with decreasing Au NP diameter, which has similar tendency with catalytic activity for CO oxidation. Moreover, the size-dependent order-to-disorder transformation of supported Au NPs is also partially rooted in the decreasing cohesive energy of the particle as the particle size decreases (*SI Appendix*, Figs. S7 and S8). Above all, the size dependences of CO adsorption energy, Au′CO extraction barrier, and Au cohesive energies give rise to the size dependence in structural responses of supported Au NPs.

The size-dependent dynamic structure of supported Au NPs under reaction condition could contribute significantly to the catalytic process. It is well known that, in heterogeneous Au catalysts, the adsorption sites of reactants such as CO and O_2 are spatially different: O_2 easily adsorbs on the CeO_2 surface defects at the perimeter of Au and CeO_2 contact (29–31), whereas CO absorbs on Au surface but not on CeO_2 surface (30, 32, 33). DFT calculations indicate a high energy barrier for CO migration on the surface of an FCC-structured gold, which does not favor low-temperature CO transport toward the absorbed O_2 (22). As such, traditional rigid models suggested that only the low-coordinated atoms on the perimeter contribute to the catalytic activity (5, 34). However, our observation clearly revealed a scenario in which ultrasmall Au nanostructures were not rigid but vigorously evolving under reaction condition, and DLCAs can be generated via CO chemisorption, which, as manifested by our simulations, enable the facile transport of CO molecules (through Au′CO) to

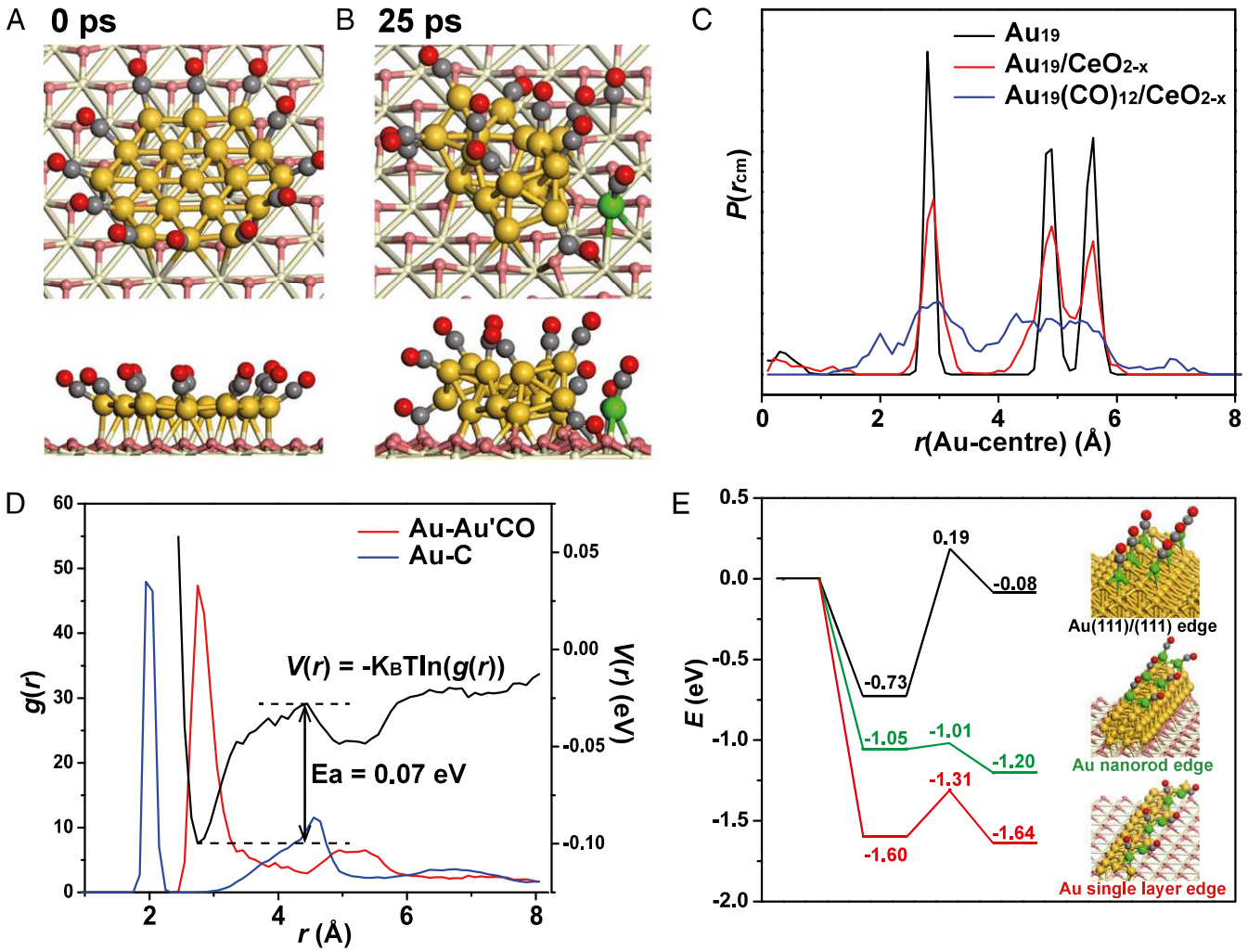

Fig. 3. Ab initio molecular-dynamics (AIMD) simulations of Au_{19} SL supported on CeO_2(111) and Au′CO extraction processes. (*A* and *B*) Initial and final configurations of the AIMD simulation of CeO_2-supported Au_{19} SL with 12 CO molecules. Color code of the spheres: Au (yellow), Ce (white), O in CeO_2 (pink), O in CO (red), C (gray), and DLCA Au (green). (*C*) The probability distribution functions $P(r_{cm})$ of the Au atoms relative to the center of mass based on >20-ps AIMD simulations at 300 K. (*D*) Radial distribution function $g_{Au\text{-}Au'CO}(r)$ and $g_{Au\text{-}CO}(r)$ and estimated mean effective potential energy path for Au′CO diffusion on $Au_{19}(CO)_{12}/CeO_{2\text{-}x}$. (*E*) Final structures and energy profile for Au′CO extraction processes with two-CO adsorption on bulk Au(111)/(111) edge, supported Au nanorod edge, and supported Au SL.

the perimeter or CeO_2 surface for the oxidation reaction (12). As such, many more Au atoms participate in the effective transport of CO to the reaction sites and hence may tremendously boost the collision rate of CO and O_2 reactants.

Conclusion

To recap, combining in situ atomic-resolution observations using ETEM and AIMD computational simulations, we have discovered a size-dependent interplay between supported Au NPs and adsorbed CO molecules. The results provide direct evidences to the activation of more atoms and generation of dynamic "single atoms" on surface (via Au′CO species) in sufficiently small Au clusters. These dynamic structural responses in ultrasmall Au clusters, presumably, boost the reaction of CO oxidation by either the facile transport of CO to active sites or single-atom catalysis, which warrants further studies. Therefore, the findings provide much-needed insights on the origin of size-dependent catalytic properties of supported gold, and demonstrate a size effect in absorbent–particle interactions that may widely exist and play an essential role in heterogeneous catalysts.

Methods

Preparation of Ceria Support. Ceria single-crystal film of 3 nm in thickness was epitaxially grown on Cu(111) surface by molecular beam epitaxy (MBE). The detailed method and condition of the MBE process can be found in our previous publication (35). The epitaxial architecture gives large atomic-flat (111) surface of ceria that is suitable for this study and guarantees stable orientation, that is, zone-axis, of the ceria crystal for continuous HRTEM. Cross-section sample was made from the Cu slab with epitaxial ceria film by saw cutting, mechanical polishing, and ion milling to electron-transparent.

In Situ Preparation of Au/Ceria Model Catalyst. The cross-section ceria sample was pasted onto a Mo ring with silver glue and loaded onto a TEM holder. The Au nanocrystals (SLs or NPs) were loaded by pressing a clean Au nanocrystal, made by fracturing a pure Au nanocrystal (36), on the ceria (111) sample surface and slowly retracting it from the contact; normally residual Au nanocrystals were left attaching on the ceria (111) surface after these maneuvers. Both the ceria sample and the Au crystal were plasma cleaned before loading into the TEM chamber, and then beam-showered in the TEM to eliminate carbon contamination.

In Situ ETEM Experiments. As schematically shown in *SI Appendix*, Fig. S1*A*, the sample assembly was loaded in an ETEM chamber (FEI Titan 80–300 with an objective lens spherical aberration corrector) operated at 300 kV, which

has a base pressure of ~10^{-8} mbar. Reactant gases (stoichiometric CO + O_2) were mixed and leaked into the ETEM chamber with pressure controlled at 10^{-4} to ~10^{-3} mbar. Gas mixing and pressure control were accomplished by a laboratory-developed auxiliary system, which is a computer-controlled system and therefore warrants a precise control of desired gas mixture and pressure. The gas composition was confirmed via a residual gas analyzer with sensitivity down to 10^{-11} mbar (near the sample area). All of the experiments were performed at room temperature.

HRTEM Image Simulation. To confirm the HRTEM contrast of the dynamically generated single Au atom, we used the DFT-calculated structure model as input to simulate the HRTEM images and compared the simulated images with the experimentally captured ones (*SI Appendix*, Fig. S2). The HRTEM image simulation of the Au NP was carried out using the multislicing method, which is integrated into the code "simulate," as is described in ref. 37. The parameters for the image simulation were chosen as follows: accelerating voltage of 300 kV and a spherical aberration coefficient of the objective lens of 2 μm.

Circumventing the (Imaging) Electron-Beam Effects. One of the major concerns regarding the in situ TEM observation is the electron beam effect. Kuwauchi et al. (20) have systematically studied electron beam effects on the intrinsic structure of Au NPs supported on TiO_2 and found that irreversible structure changes could happen for Au/TiO_2 by increasing total dose or/and electron current density. A safety zone, where the intrinsic structure of Au/TiO_2 is well preserved, has been identified to be a total dose of <1,000 A·s·cm^{-2} and an electron current density $\phi < 20$ A·cm^{-2} (20). They also found that CeO_2 is more stable than TiO_2 upon exposure to electron irradiation. Based on these results, we strictly control the electron current density to $\phi < 4$ A·cm^{-2} to minimize the beam effect. A quantitative analysis of beam dose rate effect on the dynamics of Au is provided in *SI Appendix*. Furthermore, we also carry out beam-blank experiments, as described in *SI Appendix*, Fig. S3*A*, which confirm what we observed is not dominated by electron-beam effects.

It would be generally expected that electron beam could have a detrimental effect for the adsorption of CO/O_2 on the surface of Au NP through direct knock-on mechanism and/or desorption by energy transfer from electrons. With these two factors in mind, Yoshida et al. (21) have discussed the desorption rate of CO molecule from Au NPs under beam illumination. Following their method, we estimate the maximum adsorption rate of CO molecules per surface Au atom to be ~5×10^1 s^{-1} in our working gas condition (CO: O_2 = 2:1 at 10^{-3} mbar at room temperature). The desorption rate was estimated to be 10^{-2} s^{-1} (21); thus, the adsorption rate is two orders of magnitude higher than that of desorption, indicating that dynamic adsorption of CO and structural change induced by CO can be observed in our ETEM experiments.

Computational Models. Supported Au SLs and NPs models on CeO_2(111) surface were built up to investigate their dynamic behavior under reaction condition. First, we constructed two single-layer structures that have 19 and 37 atoms, respectively, with hexagon dense-packed (111) plane of FCC Au, as shown in *SI Appendix*, Fig. S4*A*. The CeO_2(111)-p(5 × 5) and CeO_2(111)-p(6 × 6) surface slab models were used to support Au_{19} and Au_{37} SL, respectively, to avoid interaction between adjacent images. The slabs consisted of three O–Ce–O trilayers (nine atomic layers), where the bottom one O–Ce–O trilayer was frozen while the remaining layers were allowed to relax. All of the supercell slabs were repeated periodically with a 15-Å vacuum layer between the images in the direction perpendicular to the surface. Considering the extensive existence of oxygen vacancy on the CeO_2 surface, in both of the two models, we have removed one surface oxygen atom in the cell to model a partially reduced surface and located the SL above the vacancy as the initial structure of AIMD simulations.

The support effects were tested by investigating a series of supported Au nanorods on CeO_2(111)-p(3 × 5), which were used extensively to study the catalysis of supported Au NPs (22, 38). In this work, we built up Au nanorods with one and three atomic layers (*SI Appendix*, Fig. S4*B*). Note that, for three atomic layers of gold nanorod, all of the Au atoms were allowed to relax in the *y* and *z* directions, and for calculation of the Au′CO extraction process, the Au′ atom and adjacent Au atoms were allowed to fully relax.

Two types of NPs were used to calculate the cohesive energies (E_b) and the dynamic properties with CO adsorption. Supported NPs with 7–370 atoms that mimic the shape observed from ETEM photographs are shown in *SI Appendix*, Fig. S4*C*, and unsupported NPs with 20–586 atoms, which were built up by Wulff construction, are shown in *SI Appendix*, Fig. S4*D*.

Details of DFT Calculations. All of the calculations reported herein were carried out by using the Quickstep module in the CP2K simulation package (39). The wavefunction was expanded by mixed Gaussian and plane-wave basis sets with an energy cutoff of 350 Ry for the plane wave (40–42). Molecularly optimized double-ζ valence plus polarization basis sets were used to minimize the basis set superposition errors (40). Geodecker–Teter–Hutter pseudopotentials were adopted to model the core electron with 11, 12, 6, and 4 valence electrons for Au, Ce, O, and C, respectively (43). The DFT+U method was utilized in our calculations to describe the Ce 4f electrons. The value of intraatomic coulomb term minus exchange term (U – J) was chosen to be 7.0 eV to reproduce the correct band gap, gap state location, and work function (12, 42). Reciprocal space mesh consisting of gamma point was used for Brillouin zone integration. The climbing-image nudged elastic band (CI-NEB) calculations were performed to locate the saddle points with convergence criterion for the maximum force of 2×10^{-3} atomic unit. Vibrational analysis was performed to test the imaginary frequency and vibration modes to confirm the CI-NEB results (44, 45). Adsorption energies E_{ads} were calculated according to the following equation:

$$E_{ads} = E_{(slab+adsorbate)} - E_{(slab)} - E_{(adsorbate)},$$

where $E_{(slab\ +\ adsorbate)}$, $E_{(slab)}$, and $E_{(adsorbate)}$ are the calculated electronic energy of species adsorbed on the slab, the bare surface, and the gas phase molecule, respectively. Reaction energies are defined as ΔE:

$$\Delta E = E_{products} - E_{reactants}.$$

AIMD Parameters. To explore the geometry and morphology change of gold SL during reaction conditions, Born–Oppenheimer molecular dynamics (BOMD) simulations were carried out in the canonical (NVT) ensemble employing Nosé–Hoover thermostats (46, 47) with a time step of 1 fs at 300 K. Simulation of isolated Au_{19} and Au_{37} SLs were first carried out to test its stability in vacuum and reaction atmosphere. Then they were allowed to support on CeO_2(111) surface for at least 20 ps to compare the dynamic behaviors with or without CO molecules. In this work, Au_{19}/CeO_{2-x} and $Au_{19}(CO)_{12}/CeO_{2-x}$ were investigated. To test larger Au SL, Au_{37}/CeO_{2-x} and $Au_{37}(CO)_{18}/CeO_{2-x}$ were also simulated for at least 15 ps with time steps of 1 fs. (*SI Appendix*, Fig. S5) Additionally, embedded-atom model (EAM) potential was used to do classical molecular-dynamics simulations for bare isolated NPs with a time step of 2 fs, and isolated NPs with adsorbed CO were also calculated by BOMD method with a time step of 2 fs (*SI Appendix*, Fig. S8).

Radial distribution function $g(r)$ is used to study the dynamic behavior of Au–Au and Au–C bonds, and the free energy diffusion barrier for Au′CO species on Au cluster is estimated by the potential of mean force:

$$g(r) = e^{-\beta\omega^{(2)}(r)},$$

where $g(r)$ is the radial distribution function, and $\omega^{(2)}(r)$ is the average work needed to bring the two particles from infinite separation to a distance r. Thus, the potential energy surface can be estimated by the following (48, 49):

$$V(r) = \omega^{(2)}(r) = -k_B T \ln(g(r)).$$

Coverage-dependent adsorption energy per CO molecule (E_{ads}) was evaluated on a series of isolated NPs. Inasmuch as CO molecules prefer adsorbing at DLCA sites than faces (25, 26, 50, 51), CO first adsorbs on apexes sites, then edges sites, then Au(100) surface, and last Au(111) surface.

To obtain a more direct description of the dynamic behavior of the NPs, we carried out AIMD simulations for isolated NPs under 1/2 CO coverage at room temperature for more than 20 ps. The final snapshot and radial distribution function $g_{Au\text{-}Au}(r)$ are shown in *SI Appendix*, Fig. S8 *A* and *C*, respectively. To quantify the rigidity or plasticity of Au NPs with CO adsorption, we investigated the root-mean-squared bond length fluctuations (52):

$$\delta = \frac{2}{n(n-1)} \sum_{i<j} \frac{\sqrt{r_{ij}^2 - r_{ij}^2}}{r_{ij}}.$$

Thermodynamic Calculations. For reactants at a given T and P, the corresponding coverage θ can be determined by the following:

$$E_{dif}(\theta) = d[\theta \times E_{ads}]/d\theta = \Delta\mu_{CO}(T, P),$$

where $E_{dif}(\theta)$ is the differential binding energy of reactants, and $\Delta\mu_{CO}(T, P)$ is the chemical potential of CO in gas phase. Dependence of E_{ads} on θ can be estimated from the linear fitting at various particle sizes (*SI Appendix*, Fig. S7*B*). At 300 K and standard pressure, $\Delta\mu^{\varnothing}{}_{CO}(T, P^{\varnothing})$ is then given by the following (53):

$$\begin{aligned}\Delta\mu^{\varnothing}{}_{CO}(T, P^{\varnothing}) = [H(T, P^{\varnothing}, CO) - H(0\ K, P^{\varnothing}, CO)] - T[S(T, P^{\varnothing}, CO)\\ - S(0\ K, P^{\varnothing}, CO)] = [8.671\ kJ \cdot mol^{-1}]\\ - 298.15K[197.653\ J \cdot mol^{-1} \cdot K^{-1}] = -0.52\ eV.\end{aligned}$$

When CO pressure is 10^{-4} bar:

$$\Delta\mu_{CO}(T, P) = \Delta\mu^{\varnothing}{}_{CO}(T, P^{\varnothing}) + kT \ln\left(\frac{P}{P^{\varnothing}}\right) = -0.52 + 0.0257 \ln(10^{-4}) = -0.76\ eV.$$

ACKNOWLEDGMENTS. We thank Yan Wang of University of Science and Technology of China for contributing to the growth of the epitaxial CeO_2 film. The calculations were partly performed by using supercomputers at Tsinghua National Laboratory for Information Science and Technology and the Supercomputing Center of Computer Network Information Center, the Chinese Academy of Sciences. This work is supported by the Laboratory Directed Research and Development program at Pacific Northwest National Laboratory (PNNL). The work, including part of the computational calculation, was performed at the William R. Wiley Environmental Molecular Sciences Laboratory, a national user facility sponsored by US Department of Energy, Office of Biological and Environmental Research, and located at PNNL. PNNL is operated by Battelle for the US Department of Energy under Contract DE-AC05-76RLO1830. J.L. acknowledges support from the National Key Basic Research Special Foundation (2013CB834603) and National Natural Science Foundation of China (91645203, 21521091, and 21590792) of China. S.X.M. acknowledges support from the National Science Foundation (CMMI 1536811) through the University of Pittsburgh. J.Z. acknowledges support from the National Basic Research Program of China (2013CB834605) and Scientific Research and Users with Potential Grants of Hefei Science Center of Chinese Academy of Sciences (2015SRG-HSC031 and 2015HSC-UP022). Y.D. acknowledges support from the US Department of Energy, Office of Science, Office of Basic Energy Sciences, Early Career Research Program, under Award 68278.

1. Haruta M, Kobayashi T, Sano H, Yamada N (1987) Novel gold catalysts for the oxidation of carbon monoxide at a temperature far below 0 °C. *Chem Lett* 16:405–408.
2. Hutchings GJ (1985) Vapor phase hydrochlorination of acetylene: Correlation of catalytic activity of supported metal chloride catalysts. *J Catal* 96:292–295.
3. Haruta M, et al. (1993) Low-temperature oxidation of CO over gold supported on TiO_2, α-Fe_2O_3, and Co_3O_4. *J Catal* 144:175–192.
4. Haruta M (1997) Size- and support-dependency in the catalysis of gold. *Catal Today* 36:153–166.
5. Cargnello M, et al. (2013) Control of metal nanocrystal size reveals metal-support interface role for ceria catalysts. *Science* 341:771–773.
6. Valden M, Lai X, Goodman DW (1998) Onset of catalytic activity of gold clusters on titania with the appearance of nonmetallic properties. *Science* 281:1647–1650.
7. Cho A (2003) Connecting the dots to custom catalysts. *Science* 299:1684–1685.
8. Herzing AA, Kiely CJ, Carley AF, Landon P, Hutchings GJ (2008) Identification of active gold nanoclusters on iron oxide supports for CO oxidation. *Science* 321:1331–1335.
9. Liu Y, Jia CJ, Yamasaki J, Terasaki O, Schüth F (2010) Highly active iron oxide supported gold catalysts for CO oxidation: How small must the gold nanoparticles be? *Angew Chem Int Ed Engl* 49:5771–5775.
10. Li J, Li X, Zhai HJ, Wang LS (2003) Au20: A tetrahedral cluster. *Science* 299:864–867.
11. Wang J, et al. (2016) Formation, migration, and reactivity of Au-CO complexes on gold surfaces. *J Am Chem Soc* 138:1518–1526.
12. Wang YG, Mei D, Glezakou VA, Li J, Rousseau R (2015) Dynamic formation of single-atom catalytic active sites on ceria-supported gold nanoparticles. *Nat Commun* 6:6511.
13. Hrbek J, et al. (2008) Adsorbate-driven morphological changes of a gold surface at low temperatures. *J Am Chem Soc* 130:17272–17273.
14. Wang YG, Yoon Y, Glezakou VA, Li J, Rousseau R (2013) The role of reducible oxide-metal cluster charge transfer in catalytic processes: New insights on the catalytic mechanism of CO oxidation on Au/TiO_2 from ab initio molecular dynamics. *J Am Chem Soc* 135:10673–10683.
15. Tao F, et al. (2008) Reaction-driven restructuring of Rh-Pd and Pt-Pd core-shell nanoparticles. *Science* 322:932–934.
16. Hansen PL, et al. (2002) Atom-resolved imaging of dynamic shape changes in supported copper nanocrystals. *Science* 295:2053–2055.
17. Vendelbo SB, et al. (2014) Visualization of oscillatory behaviour of Pt nanoparticles catalysing CO oxidation. *Nat Mater* 13:884–890.
18. Tao FF, et al. (2016) Formation of second-generation nanoclusters on metal nanoparticles driven by reactant gases. *Nano Lett* 16:5001–5009.
19. Hammer B, Norskov JK (1995) Why gold is the noblest of all the metals. *Nature* 376:238–240.
20. Kuwauchi Y, Yoshida H, Akita T, Haruta M, Takeda S (2012) Intrinsic catalytic structure of gold nanoparticles supported on TiO_2. *Angew Chem Int Ed Engl* 51:7729–7733.
21. Yoshida H, et al. (2012) Visualizing gas molecules interacting with supported nanoparticulate catalysts at reaction conditions. *Science* 335:317–319.
22. Green IX, Tang W, Neurock M, Yates JT, Jr (2011) Spectroscopic observation of dual catalytic sites during oxidation of CO on a Au/TiO_2 catalyst. *Science* 333:736–739.
23. Wahlström E, et al. (2003) Bonding of gold nanoclusters to oxygen vacancies on rutile TiO_2(110). *Phys Rev Lett* 90:026101.
24. Esch F, et al. (2005) Electron localization determines defect formation on ceria substrates. *Science* 309:752–755.
25. Mpourmpakis G, Andriotis AN, Vlachos DG (2010) Identification of descriptors for the CO interaction with metal nanoparticles. *Nano Lett* 10:1041–1045.
26. Zhai HJ, et al. (2008) Chemisorption-induced structural changes and transition from chemisorption to physisorption in Au6(CO)n– (n = 4–9). *J Phys Chem C* 112:11920–11928.
27. Kleis J, et al. (2011) Finite size effects in chemical bonding: From small clusters to solids. *Catal Lett* 141:1067–1071.
28. Taylor MG, Austin N, Gounaris CE, Mpourmpakis G (2015) Catalyst design based on morphology- and environment-dependent adsorption on metal nanoparticles. *ACS Catal* 5:6296–6301.
29. Guzman J, Carrettin S, Corma A (2005) Spectroscopic evidence for the supply of reactive oxygen during CO oxidation catalyzed by gold supported on nanocrystalline CeO_2. *J Am Chem Soc* 127:3286–3287.
30. Carrettin S, Concepción P, Corma A, López Nieto JM, Puntes VF (2004) Nanocrystalline CeO_2 increases the activity of Au for CO oxidation by two orders of magnitude. *Angew Chem Int Ed Engl* 43:2538–2540.
31. Wu Z, Li M, Howe J, Meyer HM, 3rd, Overbury SH (2010) Probing defect sites on CeO_2 nanocrystals with well-defined surface planes by Raman spectroscopy and O_2 adsorption. *Langmuir* 26:16595–16606.
32. Baron M, Bondarchuk O, Stacchiola D, Shaikhutdinov S, Freund HJ (2009) Interaction of gold with cerium oxide supports: CeO_2 (111) thin films vs CeO_x nanoparticles. *J Phys Chem C* 113:6042–6049.
33. Kim HY, Lee HM, Henkelman G (2012) CO oxidation mechanism on CeO_2)-supported Au nanoparticles. *J Am Chem Soc* 134:1560–1570.
34. Wu CY, et al. (2017) High-spatial-resolution mapping of catalytic reactions on single particles. *Nature* 541:511–515.
35. Hu S, et al. (2015) Ag nanoparticles on reducible CeO_2(111) thin films: Effect of thickness and stoichiometry of ceria. *J Phys Chem C* 119:3579–3588.
36. Zheng H, et al. (2010) Discrete plasticity in sub-10-nm-sized gold crystals. *Nat Commun* 1:144.
37. Gómez-Rodríguez A, Beltrán-Del-Río LM, Herrera-Becerra R (2010) SimulaTEM: Multislice simulations for general objects. *Ultramicroscopy* 110:95–104.
38. Song W, Hensen EJ (2014) Mechanistic aspects of the water–gas shift reaction on isolated and clustered Au atoms on CeO_2 (110): A density functional theory study. *ACS Catal* 4:1885–1892.
39. VandeVondele J, et al. (2005) Quickstep: Fast and accurate density functional calculations using a mixed Gaussian and plane waves approach. *Comput Phys Commun* 167:103–128.
40. VandeVondele J, Hutter J (2007) Gaussian basis sets for accurate calculations on molecular systems in gas and condensed phases. *J Chem Phys* 127:114105.
41. Lippert BG, Hutter J, Parrinello M (1997) A hybrid Gaussian and plane wave density functional scheme. *Mol Phys* 92:477–488.
42. Wang YG, Mei D, Li J, Rousseau R (2013) DFT+U study on the localized electronic states and their potential role during H_2O dissociation and CO oxidation processes on CeO_2(111) surface. *J Phys Chem C* 117:23082–23089.
43. Goedecker S, Teter M, Hutter J (1996) Separable dual-space Gaussian pseudopotentials. *Phys Rev B Condens Matter* 54:1703–1710.
44. Henkelman G, Uberuaga BP, Jónsson H (2000) A climbing image nudged elastic band method for finding saddle points and minimum energy paths. *J Chem Phys* 113:9901–9904.
45. Mills G, Jónsson H, Schenter GK (1995) Reversible work transition state theory: Application to dissociative adsorption of hydrogen. *Surf Sci* 324:305–337.
46. Hoover WG (1985) Canonical dynamics: Equilibrium phase-space distributions. *Phys Rev A Gen Phys* 31:1695–1697.
47. Nosé S (1984) A unified formulation of the constant temperature molecular dynamics methods. *J Chem Phys* 81:511–519.
48. Kirkwood JG (1935) Statistical mechanics of fluid mixtures. *J Chem Phys* 3:300–313.
49. Kirkwood JG (1936) Statistical mechanics of liquid solutions. *Chem Rev* 19:275–307.
50. Molina L, Hammer B (2004) Theoretical study of CO oxidation on Au nanoparticles supported by MgO (100). *Phys Rev B* 69:155424.
51. Molina L, Hammer B (2005) Some recent theoretical advances in the understanding of the catalytic activity of Au. *Appl Catal A Gen* 291:21–31.
52. Beck TL, Doll J, Freeman DL (1989) The quantum mechanics of cluster melting. *J Chem Phys* 90:5651–5656.
53. Chase MW, Jr, et al. (1985) *JANAF Thermochemical Tables, Third Edition*. Journal of Physical and Chemical Reference Data Supplement (National Institute of Standards and Technology, Gaithersburg, MD), Vol 14, Suppl 1.